RESEARCH ARTICLE

Key Points:
- Background solar wind speed is an important parameter in the propagation of IP shocks/CMEs
- Prediction of the ICME/shock arrival time at 1 AU can be more problematic for slow than fast CMEs
- A long period of simulation is necessary to make solar source geomagnetic storm associations

Correspondence to:
C.-C. Wu,
chin-chun.wu@nrl.navy.mil

Numerical simulation of multiple CME-driven shocks in the month of 2011 September

Chin-Chun Wu[1], Kan Liou[2], Angelos Vourlidas[2], Simon Plunkett[1], Murray Dryer[3], S. T. Wu[4], Dennis Socker[1], Brian E. Wood[1], Lynn Hutting[1], and Russell A. Howard[1]

[1]Naval Research Laboratory, Washington, District of Columbia, USA, [2]Applied Physics Laboratory, Laurel, Maryland, USA, [3]Space Weather Predictions Center, Emeritus, NOAA, Boulder, Colorado, USA, [4]CSPAR, University of Alabama in Huntsville, Huntsville, Alabama, USA

Abstract A global, three-dimensional (3-D) numerical simulation model has been employed to study the Sun-to-Earth propagation of multiple (12) coronal mass ejections (CMEs) and their associated shocks in September 2011. The inputs to the simulation are based on actual solar observations, which include the CME speeds, source locations, and photospheric magnetic fields. The simulation result is fine tuned with in situ solar wind data observations at 1 AU by matching the arrival time of CME-driven shocks. During this period three CME-driven interplanetary (IP) shocks induced three sizable geomagnetic storms on 9, 17, and 26 September, with Dst values reaching -69, -70, and -101 nT, respectively. These storm events signify the commencement of geomagnetic activity in the solar cycle 24. The CME propagation speed near the Sun (e.g., $< 30 R_S$) has been widely used to estimate the interplanetary CME (ICME)/Shock arrival time at 1 AU. Our simulation indicates that the background solar wind speed, as expected, is an important controlling parameter in the propagation of IP shocks and CMEs. Prediction of the ICME/shock arrival time at 1 AU can be more problematic for slow (e.g., < 500 km s^{-1}) than fast CMEs (>1000 km s^{-1}). This is because the effect of the background solar wind is more pronounced for slow CMEs. Here we demonstrate this difficulty with a slow (400 km s^{-1}) CME event that arrived at the Earth in 3 days instead of the predicted 4.3 days. Our results also demonstrate that a long period (a month in this case) of simulation may be necessary to make meaningful solar source geomagnetic storm associations.

1. Introduction

Since 1957, the start of recording Dst (index of geomagnetic activity), the yearly Dst_{min} (minimum Dst) has always been less than -80 nT until 2007. No large geomagnetic storm (e.g., $Dst_{min} < -80$ nT) was recorded during 2007–2009, due to the low solar activity. For example, the yearly average occurrence rates of magnetic clouds (MCs) and magnetic cloud-like structures (MCLs) were 9.3 and 10.9 during 1995–2012, but no MCL and only one MC was observed in 2008 [e.g., *Wu and Lepping*, 2015]. The sunspot number was extremely low during 2007–2009. Southward interplanetary magnetic field (IMF) or B_z play a major role in causing geomagnetic storms [e.g., *Tsurutani et al.*, 1988; *Tsurutani and Gonzalez*, 1997]. MCs are one of the major solar wind structures that contain a long lasting southward IMF [e.g., *Burlaga et al.*, 1981]. Approximately 90% of MCs are associated with geomagnetic storms [e.g., *Wu and Lepping*, 2002a, 2002b, 2011, 2015]. There were 4, 1, and 12 MCs observed in 2007, 2008, and 2009, respectively [*Lepping et al.*, 2011] but no large geomagnetic storm associated with these MCs. Dst_{min} were -70, -72, -79 nT in 2007, 2008, and 2009, respectively.

After an extremely long period of low solar activity during the years 2007–2009, the Sun became more active when the new solar cycle began in 2010. Many nonrecurrent solar disturbances (e.g., coronal mass ejections (CMEs)) were observed in 2010. Some of them induced sizable geomagnetic storms. The first sizeable geomagnetic storm ($Dst_{min} < -80$ nT) in solar cycle 24 occurred on 6 April 2010, which was associated with a CME event on 3 April 2010 [e.g., *Wood et al.*, 2011]. The first multiple CMEs event occurred in August 2010, which caused a geomagnetic storm on 3 August [e.g., *Wu et al.*, 2011; *Möstl et al.*, 2012]. Since then, more sizeable geomagnetic storms associated with multiple CME events have been recorded. For example, four CMEs were launched near the time of the geomagnetic storm on 10 March 2011 [*Wood et al.*, 2012].

The first severe geomagnetic storms (with $Dst_{min} < -100$ nT) in solar cycle 24 occurred during 05–06 August 2011, and the second and third severe geomagnetic storms occurred during 26–27 September 2011 and 24–25 October 2011, respectively. Five severe geomagnetic storms were recorded in 2012, but only two
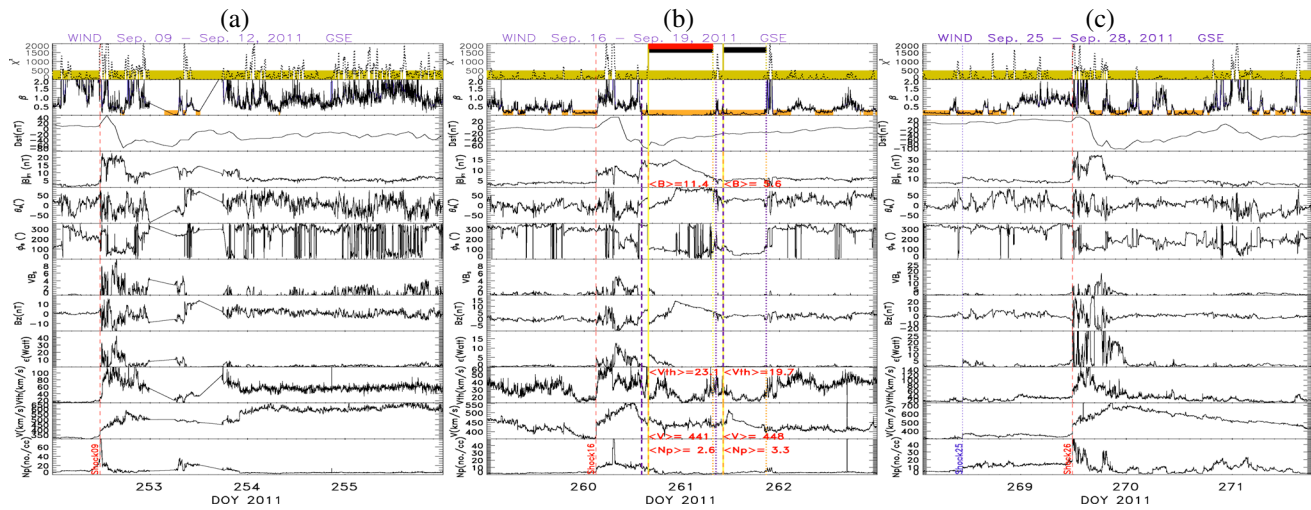
Figure 1. Profiles of magnetic field and plasma parameters for solar wind during (a) 9–12, (b) 16–19, and (c) 25–28 September 2011, in terms of (from top to bottom) χ^2 of a quadratic fit to latitude of the field (θ_B), running average of proton plasma beta (β) and dotted curve representing its running average, Dst, magnetic field in terms of magnitude, latitude (θ_B) and longitude (ϕ_B) in GSE coordinate system, induced electric field (VB_S), B_z of the field in GSE, solar wind magnetosphere energy coupling function ε [see, *Akasofu*, 1981], proton plasma thermal speed (V_{th}), bulk speed (V), and number density (N_P). The red horizontal bar in the twelfth panel in Figure 1b represents the scheme's identification of the extent of this MC candidate [*Lepping et al.*, 2015a]. Green horizontal bar represent χ^2 was less than 500. In Figure 1b, yellow dashed line and blue dotted line represent front and rear boundaries identified by MC automatic identify model. Averages of Np, V, V_{th}, and B for MC/MCL are provided in red in each panel. A magnetic cloud-like structure (MCL) was observed on 17 September 2011.

severe geomagnetic storms were recorded in 2013. In the early phase of solar cycle 24, the most intense storm occurred during 07–08 March 2012. The storm's Dst_{min} was $-143\,nT$.

During low solar activity, only a small fraction of MCs have driven interplanetary (IP) shocks in front of the MCs [e.g., *Lepping et al.*, 2011, 2015b; *Wu and Lepping*, 2016]. Three sudden storm commencements (SSCs) were recorded in September 2011. These three SSCs were caused by IP shocks. This was the first time that three IP shock-associated geomagnetic storms were recorded within a month in solar cycle 24. Figure 1 shows *Wind* observed solar wind density, velocity, thermal speed (first to third rows from bottom), magnetic field (fifth and seventh to ninth rows), solar wind magnetosphere energy coupling function of Akasofu (ε; fourth panel), induced electric field (VB_S; sixth row), plasma β (eleventh row), and Dst (tenth row). Vertical red dashed lines mark the timing of IP shocks. It is clear that SSCs followed the responsible IP shocks (see Dst panel.)

Geomagnetic storms are one of the most important topics in space physics. The arrival of an IP shock at the Earth produces the first signature of a geomagnetic storm. Numerical simulation can play an important role in predicting the shock arrival [e.g., *Manchester et al.*, 2004; *Odstrcil et al.*, 2005; *Wu et al.*, 2007a, 2007b; *Hayashi et al.*, 2011; *Shen et al.*, 2011a; *Xiong et al.*, 2006a]. Some 3-D MHD models can produce simulated results that match the in situ observations at 1 AU [e.g., *Manchester et al.*, 2004; *Odstrcil et al.*, 2005; *Wu et al.*, 2007a, 2007b, 2011, 2012, 2016; *Lugaz and Roussev*, 2011; *Shen et al.*, 2011a, 2014a; *Wood et al.*, 2011; *Liou et al.*, 2014]. Because the Sun is always evolving and solar disturbances, when propagating outward, can interact with the solar wind and with each other depending on their properties [e.g., *Wu et al.*, 2007a, 2007b, 2012, 2016], predicting their geomagnetic effects is difficult, especially for multiple solar events [e.g., *Xiong et al.*, 2006a, 2007]. For example, background magnetic field, coronal hole, and solar wind may change the propagation direction of CMEs [e.g., *Gopalswamy et al.*, 2009; *Shen et al.*, 2011b; *Zhou and Feng*, 2013; *Wang et al.*, 2014] which may also influence the geoeffectiveness of interplanetary CMEs (ICMEs). Therefore, we are motivated to study the long-term evolution/interaction of the multiple CMEs en route to the Earth.

The 12 CME events and three geomagnetic storm events in September 2011 provide a good example of a complex association between the solar and geomagnetic events. In order to understand the association of the three geomagnetic storms, a global 3-D, time-dependent, MHD model [*Wu et al.*, 2007a, 2007b] is employed to simulate these three IP shocks and the evolution/interaction of multiple CMEs during 6–30 September 2011. The MHD simulation model and data analysis will be presented in sections 2 and 3. Simulation results and data validation will be presented in section 4. Discussion and Conclusion will be presented in sections 5 and 6.

2. Numerical Simulation Models

A well-established global 3-D simulation model [*Wu et al.*, 2007a, 2007b] is used for this study. The model is capable of simulating realistic background solar wind profiles as well as solar disturbances (e.g., CMEs/ICMEs) from the surface of the Sun to the Earth and beyond. The numerical simulation uses the observed line-of-sight magnetic field at the photosphere extrapolated to 2.5 R_S by the Wang-Sheeley-Arge (WSA) model [*Wang and Sheeley*, 1990a, 1990b; *Arge and Pizzo*, 2000]. Our model combines two simulation codes: the Hakamada-Akasofu-Fry code (HAFv.2) [see also *Fry et al.*, 2001, and references therein] and a fully 3-D, time-dependent MHD simulation code [*Han et al.*, 1988; *Detman et al.*, 1991]. We will refer to our model as "H3DMHD" (where "H" refers to "hybrid"). HAFv.2 is a physics-based kinematic model that uses a modified kinematic approach to simulate the solar wind conditions out to 18 R_S with data from Carrington Rotation maps (2.5 R_S), provided by NOAA's Space Weather Prediction Center (http://swpc.noaa.gov), as the input. The output of HAFv.2 at 40 R_S (0.18 AU) provides input for the time-dependent 3-D MHD solar wind model. The system is driven by a time series of synoptic photospheric magnetic maps composed from daily solar photospheric magnetograms (http://wso.stanford.edu). Use of these data to provide solar wind velocity and the initially radial IMF at 2.5 R_S is described in previous studies [e.g., *Wang and Sheeley*, 1990a, 1990b, 1992; *Arge and Pizzo*, 2000].

An extension of the two-step Lax-Wendroff finite difference methods [*Lax and Wendroff*, 1960] is used in this numerical 3-D MHD scheme, and the model solves the basic conservation of mass and energy, equation of motion, and induction equation [*Han*, 1977]. The specific heat ratio, $\gamma = 5/3$, is used for this study since it is a better value to use for in situ solar wind data at 1 AU [e.g., *Wu et al.*, 2011; *Liou et al.*, 2014].

The computational domain for the 3-D MHD simulation is a sun-centered spherical coordinate system (r, θ, and ϕ) oriented on the ecliptic plane. Earth is located at $r = 215\,R_S$, $\theta = 0°$, and $\phi = 180°$. The domain covers $-87.5° \leq \theta \leq 87.5°$; $0° \leq \phi \leq 360°$; $40\,R_S \leq r \leq 346\,R_S$. An open boundary condition at both $\theta = 87.5°$ and $\theta = -87.5°$ is used so there are no reflective disturbances. A constant grid size of $\Delta r = 3\,R_S$, $\Delta\theta = 5°$, and $\Delta\phi = 5°$ is used which results in $103 \times 36 \times 72$ grid sets.

3. Data Analysis: Solar Wind Condition and CME Events in September 2011

Three SSCs were recorded in September 2011. These three SSCs were induced by three individual IP shocks. This was the first occurrence of three IP shock-associated geomagnetic storms in a month for solar cycle 24. Figure 1 shows solar wind plasma, magnetic field, and other derived parameters at the Libration point, L1, as discussed above. Vertical red dashed lines mark the timing of IP shocks. The tenth row (from the bottom) shows the geomagnetic activity index (*Dst*). These three storms are all caused by southward IMF (B_z) in the sheath (region behind the IP shocks and ahead of the solar ejecta). Only the IP Shock17 ("17": IP shock observed on 17 September) was followed by a magnetic cloud (MC). No MC or MC-like structure (MCL) followed Shock09 ("09": IP shock observed on 9 September) or Shock26 ("26": IP shock observed on 26 September). The intensities of geomagnetic storms associated with Shock09, Shock17, and Shock26, are -60, -70, and -101 nT, respectively.

Shock09 is not a strong shock because the jump (difference between upstream and downstream) conditions for velocity, thermal speed, and magnetic field are small. The method used to identify the shock is based on the earlier studies [e.g., *Wu et al.*, 1996, 2004, 2006a, 2006b]. For example, the velocity increases from 300 to 350 km s^{-1}, the thermal speed increases from ~20 to 25 km s^{-1}, the magnetic field increases from ~5 to 7 nT, and the density increases from 20 to 40 cm^{-3} (see Figure 2a). Behind the Shock09, a sharp increase of magnetic field (B increases from ~2 nT to ~20 nT), and a sharp decrease of density (Np dropped from ~80 to ~10 cm^{-3}) about ~20 min after the Shock09 was recorded by the Wind spacecraft at L1. The magnetic field rotates twice between the two vertical (red dashed and blue dotted) lines, but both temperature (thermal speed) and proton velocity are almost constant. This kind of structure is called a "magnetic cavity" or a "magnetic hole (MH)" which has low magnetic field and high density near the centre of the hole. The front boundary of MH09 (the magnetic hole observed on 9 September 2011) is connected to the Shock09. Shock17 was followed by another magnetic hole, MH17 which was observed ~4.8 h after Shock17 passed the Wind spacecraft. In the centre of the MH17, B is ~4 nT, and Np is ~60 cm^{-3} (see Figure 2b). There is no magnetic hole following Shock26 (Figure 2c), but the magnetic field rotates. We will discuss this point in section 5 in the context of the heliospheric current sheet configuration.
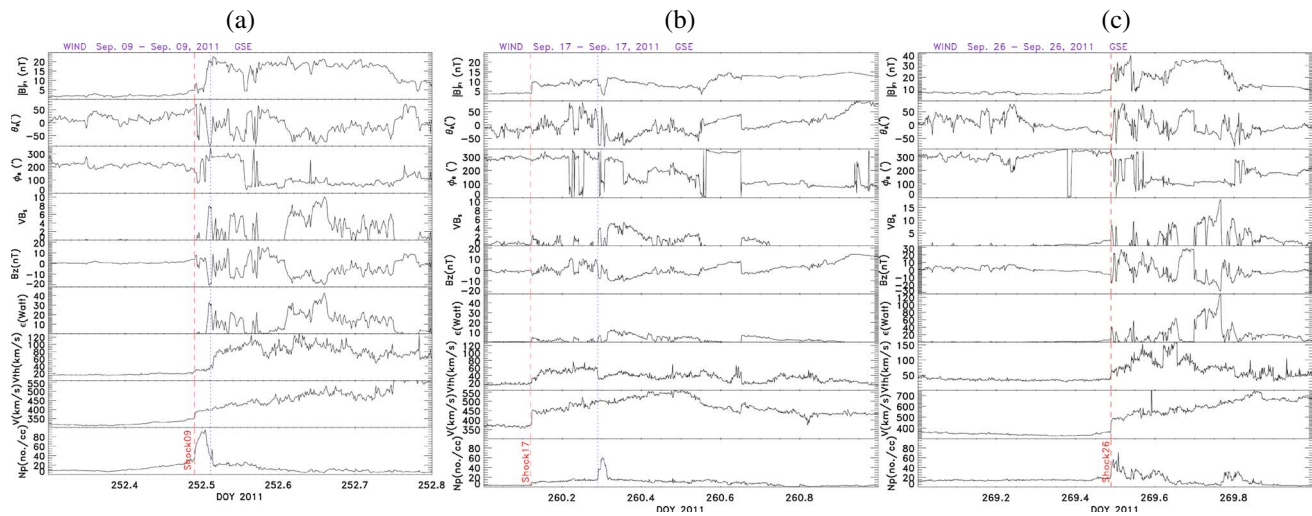
Figure 2. (bottom to top) Solar wind proton density, velocity, thermal speed (or temperature), derived parameters of Akasofu ε, z component of IMF (B_z), VB_S, ϕ_B, θ_B, and IMF B on (a) 9 September, (b) 17 September, and (c) 26 September. Vertical red dashed lines marked the arrival times of IP shocks at Wind spacecraft. Shock09, Shock17, and Shock26 mean IP shock observed on 9, 17, and 26 September 2011.

It is well known that most IP shocks (observed at 1 AU) are driven by CMEs. It takes about 1–6 days for a CME to propagate from its birth place (e.g., near the surface of the Sun) to the Earth environment. The CME events that erupted a few days before Shock09, Shock17, and Shock26 are the candidates for generation of these three IP shocks. However, many CMEs erupted in September 2011. We are able to identify 12 CMEs (speed and source location) from *STEREO* images during 2–24 September 2011. These CME images are shown in Figure 3, and related information is listed in Table 1. COR2 images are used to estimate the speed of CMEs, and STEREO EUV Imager images or flare reports are used to identify the source locations of CMEs.

The CME (Figure 3b) that erupted at 2239 UT from AR11283 at N14W18 on 6 September generated Shock09 (see section 5.1). Based on the Sun-Earth Connection Coronal and Heliospheric Investigation (SECCHI)/COR2A observations, we derive an averaged CME speed of ~1230 km s^{-1} which is about 2 times higher than the speed derived from Large Angle and Spectrometric Coronagraph observations (~570 km/s as reported in the Coordinated Data Analysis Workshop list, http://cdaw.gsfc.nasa.gov/CME_list/). This is expected since the CME is Earth directed and hence propagates close to the sky plane of COR2A. The CME (Figure 3f) that erupted with a propagation speed of ~408 km s^{-1} at 0000 UT from AR11289 at N22W14 on 14 September generated Shock17 (see section 5.2). The two CMEs (Figures 3k and 3l) that erupted at 1250 UT and 1948 UT from AR11283 at N12E60 on 24 September generated Shock26 (see section 5.3). The CMEs propagation speeds are ~1050 and 1065 km s^{-1}, respectively.

4. Validation and Comparison of Global H3DMHD Simulation Results With Observation

It is important to validate the simulation results. Validation of our simulation results is done by comparing solar wind plasma and field parameters with in situ measurements made by Wind. We use photospheric observations that are extrapolated to 2.5 R_S by the WSA model [*Wang and Sheeley*, 1990a, 1990b; *Arge and Pizzo*, 2000] and the CME observations as the initial conditions to drive the corotating background solar wind plasma and IMF conditions of the simulation code.

To initialize the simulation, we input the three components of magnetic field and radial velocity field together with density from the HAFv.2 model at 40 R_S into our H3DMHD model to compute all physical parameters to 215 R_S and beyond (e.g., the outer boundary of the simulation is at 346 R_S, ~1.67 AU). There is no observation available at 40 R_S. Observed in situ solar wind (e.g., Wind/*ACE*) is used to validate the simulation results. For the inner boundary set at 2.5 R_S, density = 5.3 × 10^4 cm^{-3}. We justify setting density constant on the source surface because, by doing so, it allows the modified kinematic procedure in HAF2 to produce fairly
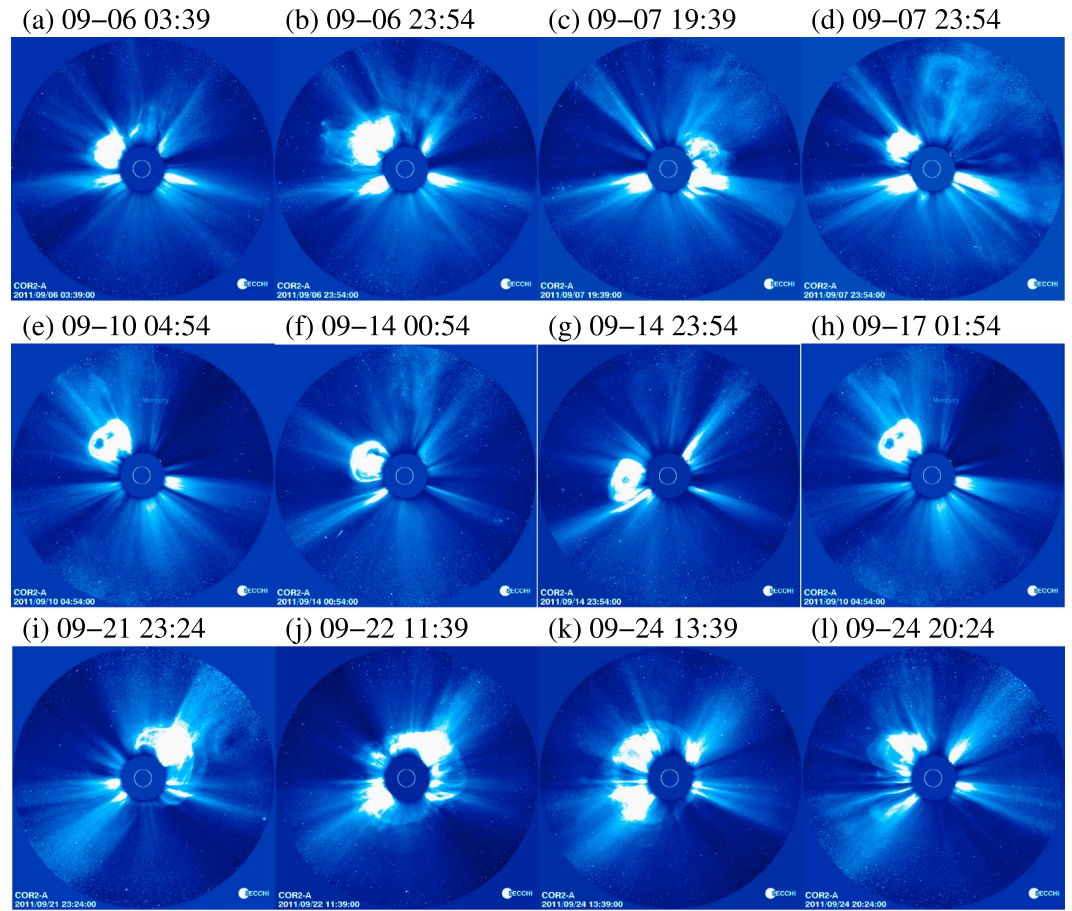
Figure 3. CMEs observed by COR2-A during 6–24 September 2011, respectively.

representative density variations and values at 1 AU compared with coincident L1 data. The MHD simulation gives the nonradial velocities. In the 3-D MHD simulation, we set a relaxation time for 6 days (or 144 h) for getting an undisturbed background solar wind condition. In this study, we added 12 solar disturbances (velocity pulses for simulating CMEs) into the lower boundary (2.5 R_S) according to the speeds measured from STEREO COR2 images which are listed in Table 1.

Table 1. Eruption Time, Location, and Propagation Speed of CMEs During 6–24 September 2011

CME#	Date	Time (UT)	Source Location	Speed (km s^{-1})
CME06a	0906	0224	N14W07	312
CME06b[a]	0906	2239	N14W18	570
CME07a	0907	1854	N23E54	657
CME07b	0907	2254	N14W28	681
CME10	0910	0335	N33W28	632
CME14a[b]	0914	0154	N22W03	400
CME14b	0914	2154	S15W45	400
CME17	0917	0039	N21W52	499
CME21	0921	2254	N23W115	620
CME22	0922	1124	N08E78	1020
CME24a[c]	0924	1254	N12E60	1050
CME24b[c]	0924	1948	N12E60	1065

[a]Ccorresponding to Shock09.
[b]Corresponding to Shock17.
[c]Corresponding to Shock26.
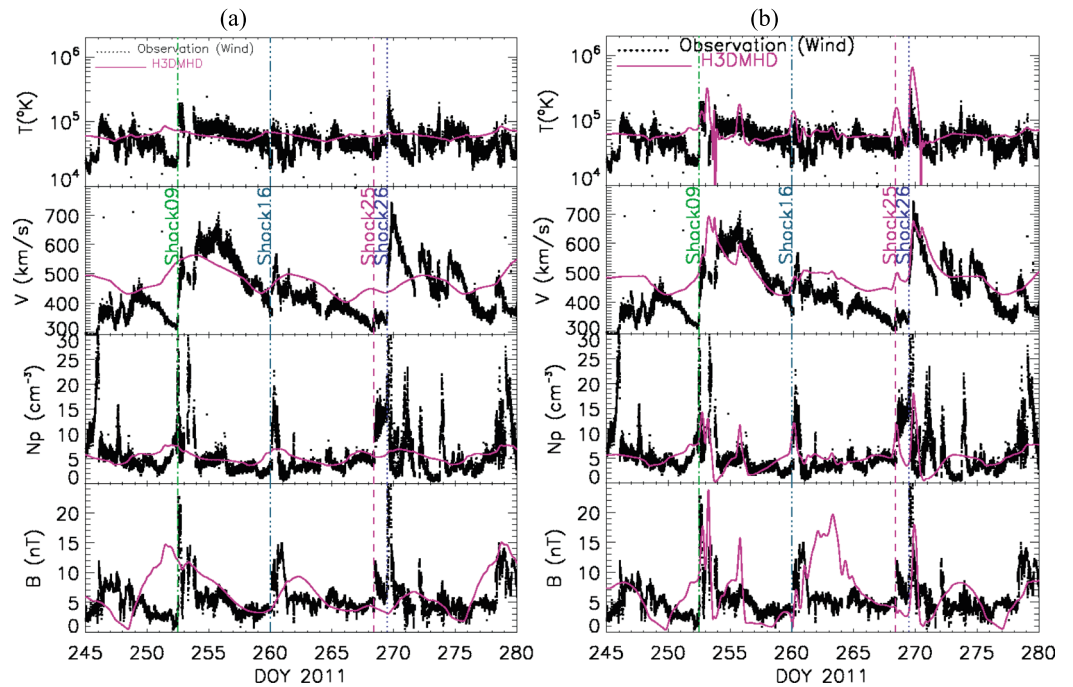
Figure 4. Time profile of solar wind magnetic field (*B*), density (*Np*), velocity (*V*), and temperature (*T*) during 1 September to 6 October 2011 recorded by Wind spacecraft (black dotted lines) and simulated by H3DMHD model (pink solid lines). Vertical lines indicated the interplanetary shock observed by Wind. (a) Results using initial input conditions without CME inputs at 2.5 R_S. (b) Results using 12 CMEs final input tuning conditions as noted in the text.

Figure 4a shows a comparison of the simulated background solar wind (from H3DMHD in pink solid lines) with observation (from Wind in black dotted lines) for the period between 1 September and 8 October. The vertical lines indicate arrival time of IP shocks (at Wind or 1 AU) on 9, 17, 25, and 26 September, respectively. The labels "Shock09," "Shock17," "Shock25," and "Shock26" mean that IP shocks arrived at the Wind spacecraft on 9, 17, 25, and 26 September, respectively. The time resolution of the observations is ≈ 1.5 min. The time resolution of simulated solar wind is in a range of ≈ 1 to ≈ 15 min, which depends on the simulated solar wind condition.

The CME itself is produced by introducing a pressure pulse (a velocity pulse is one kind of pressure pulse) at the inner boundary ($r = 2.5\,R_S$) at the time and location of the flare associated with the event (i.e., at 22:39 UT, at a position S14W18 relative to the Sun-Earth axis for CME06b). The pressure pulse consists of a 5 min exponential rise in wind velocity to a peak then decay back to the original value. The speed's highest value is at the source location and decreases with angular distance from that location. The rate of falloff is specified by the sigma angle, defined as the great circle angle where the radial speed falls to ½ the speed at the centroid (flare site). Using HAF code, the duration and amplitude of the velocity pulse are the two free parameters to match the arrival time of the CME-driven shock and the CME profile at Earth. For example, velocity pulse with longer duration or higher speed will pump more energy into the system; thus, the CME-driven shock will arrive at the Earth earlier. Velocity perturbations for 12 CME events were added into the simulation. Table 1 lists the detailed information about source location, eruption time, and propagation speed of these CMEs. We tuned the solar disturbances' duration and velocity amplitude to match the arrival time of solar wind structures (e.g., IP shocks) at 1 AU. Figure 4b (final tuning procedure's result) shows the comparison of 1 AU solar wind parameters for observation (black curves) versus simulation (pink solid lines). V_{peak} (peak of solar wind velocity) downstream of the IP shocks matched well for the IP shocks on 17 September and 26 September but was a little bit high for the shock on 9 September. B_{peak} (peak of IMF) and Np_{peak} (peak of solar wind density) downstream of the IP shocks are also reasonably well matched. No simulated IP shock was formed in Figure 4a, because no simulated CME perturbation is added into the lower boundary (2.5 R_S).

Figures 5a and 5b show the background (corotating "steady state") solar wind condition at 40 and 214 R_S (from the left to the right), respectively at 0000 UT on 3 September 2011. The solar wind condition at the lower boundary (40 R_S) is super Alfvenic. Latitude is in the vertical direction and longitude is in the horizontal

(a)   (b)
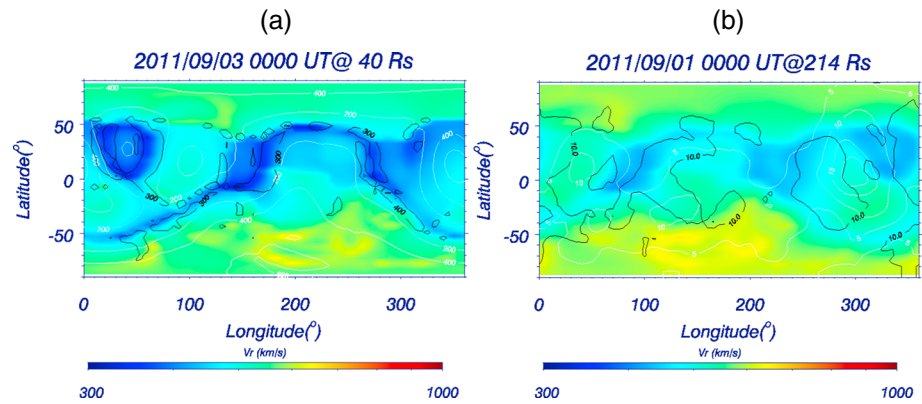
**Figure 5.** Background (corotating steady state) solar wind condition at (left) 40 and (right) 214 R_S, respectively, at 0000 UT on 3 September 2011. Colors represent the variation of solar wind velocity in the r direction (V_r), black contour lines represent solar wind density (unit in no./cm^3), and white contour lines represent IMFs (nT).

direction. Earth is located near the center of Figure 5b, at heliolongitude, $\phi = 180°$, and at latitude, $\theta = 7°$. Colors represent the variation of solar wind velocity in the r direction (V_r), black contour lines represent solar wind density (units in no./cm^3), and white contour lines represent the IMF (units in nT). The heliospheric current sheet is clearly not flat (see the blue color of the lower velocity horizontal band near the equator).

Figure 6 shows undisturbed solar wind speed on surfaces of angular cones that are centered at the Sun's center. The central red dot represents the Sun, and the blue circle indicates the location of 1 AU. These conical angles (Figures 6a–6c) are at 22.5°N (north); 12.5°N, close to the latitude of the source locations of CME06a and CME06b; and 7.5°N, close to Earth's latitude, in the solar equatorial system. Also plotted (Figures 6d–6e) are at 12.5°S and 22.5°S, representative of a response in the southern heliosphere. It is clear that the solar wind speed is faster in the Southern Hemisphere (Figures 6d–6e) than in the Northern Hemisphere (Figures 6a and 6b). Figure 6 shows a highly nonuniform distribution of solar wind speed, notably the coronal hole high-speed stream west of the Earth. Near the solar equatorial plane (see Figure 6c), Earth was surrounded by lower speed solar wind. Three light-blue-yellow spiral bands indicate corotating interaction regions (CIRs) which are about ~120° apart. The heliosphere was divided into three sectors by the CIRs. These CIRs have higher speed flows located at the east sector in the Northern Hemisphere. In the Southern Hemisphere, the highest speed was near the Sun-Earth line direction (heliospheric $\phi = 0°$). Overall, the solar wind speed is faster at higher latitudes than in the equatorial regions, and the highest speed solar wind comes from the eastern sector (~90° apart from the Sun-Earth line plane) of the Northern Hemisphere (see the light yellow band in Figures 6b and 6c and velocity color contours in Figure 6).

Figure 7 shows daily plots of simulated solar wind velocity in the meridian plane (at Sun-Earth line, or at longitude = 180° for Earth in this figure) during 3 September to 4 October 2011. Figure 8 shows daily plots of simulated solar wind velocity near the solar equator plane (latitude = 7.5°, or 7.5°N) during 7–30 September 2011 at

(a)   (b)   (c)   (d)   (e)
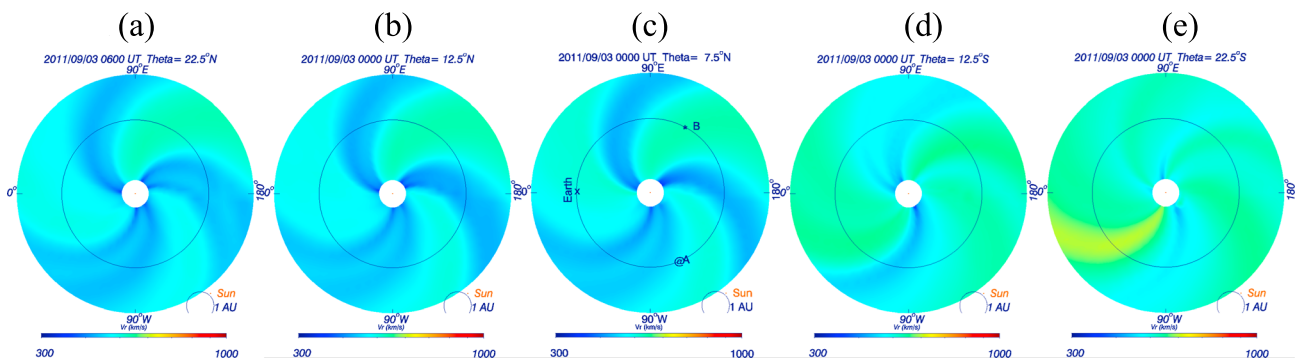
Figure 6. Undisturbed solar wind velocity on surfaces of angular cones that are centered at the Sun's center. These conical angles are at 22.5°N; 12.5°N: close to the first actual flare's latitude; 7.5°N: close to Earth's latitude in the solar equatorial coordinate system; and 12.5°S, and 22.5°S.
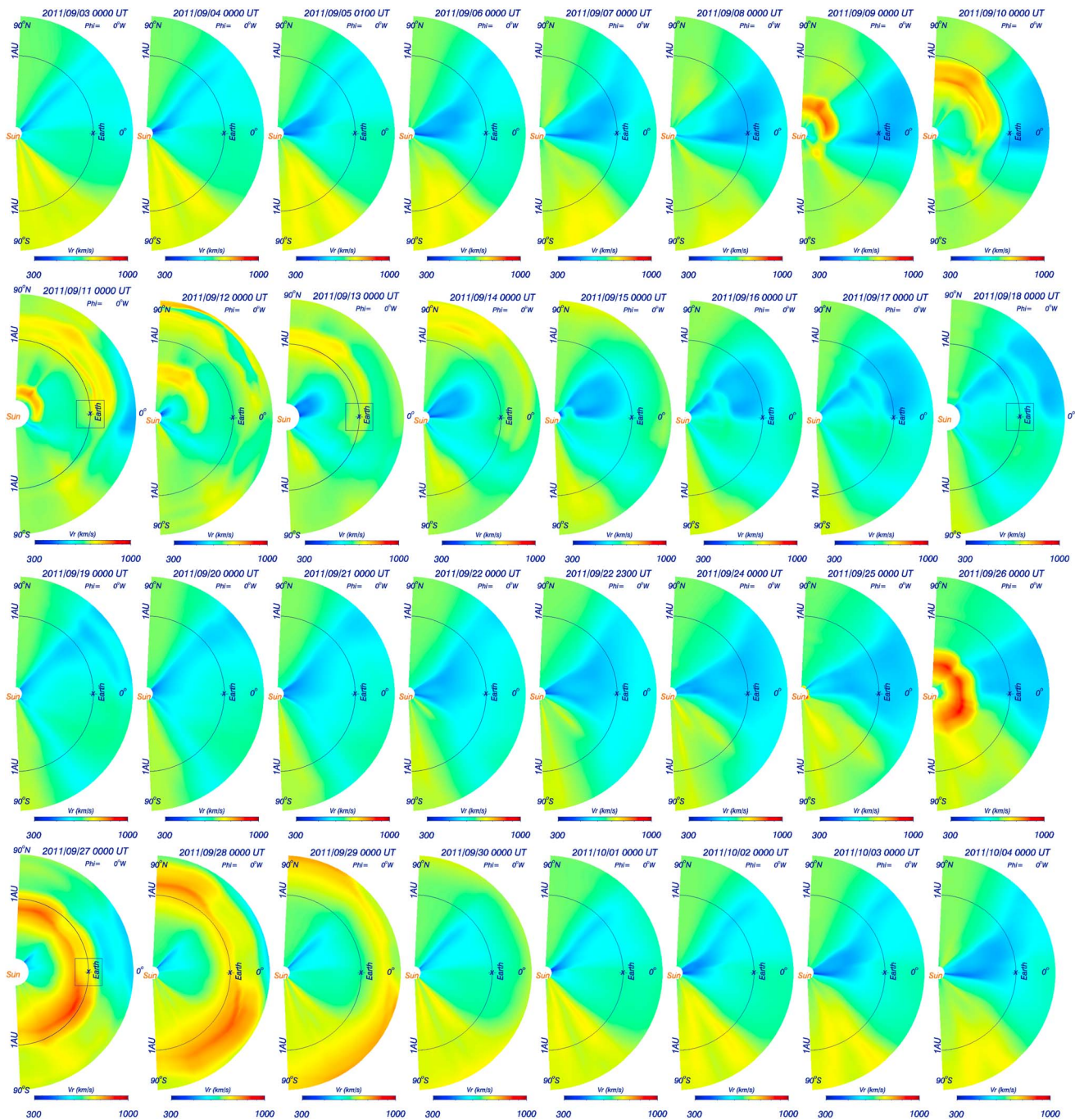
Figure 7. Daily plot of simulated solar wind velocity in the meridian plane (at Sun-Earth line or at longitude = 180° during 3 September 2011 to 4 October 2011). Note that Earth is at longitude = 180° in this figure.

longitude = 0° in this figure. Figures 7 and 8 show clearly that a high-speed structure (or CME/IP shock, see the velocity inside the blue squares) has passed over the Earth on 11, 13, 18, and 27 September.

The solar wind speed is highly nonuniform in the latitude profile, which is shown clearly in Figure 7. For example, the speed is slower at the equator than in the higher latitude region. The background solar wind speed is one of the major factors that can affect the propagation of CMEs [e.g., *Wu et al.*, 2007a, 2007b, 2011; *Shen et al.*, 2014b]. Due to the nonuniform distribution of the background solar wind speed, the CME velocity profile was highly asymmetric as shown in Figure 7. In addition, the speed in the south is faster than in the north. The leading edges of the CMEs are located in the regions with faster solar wind speed.
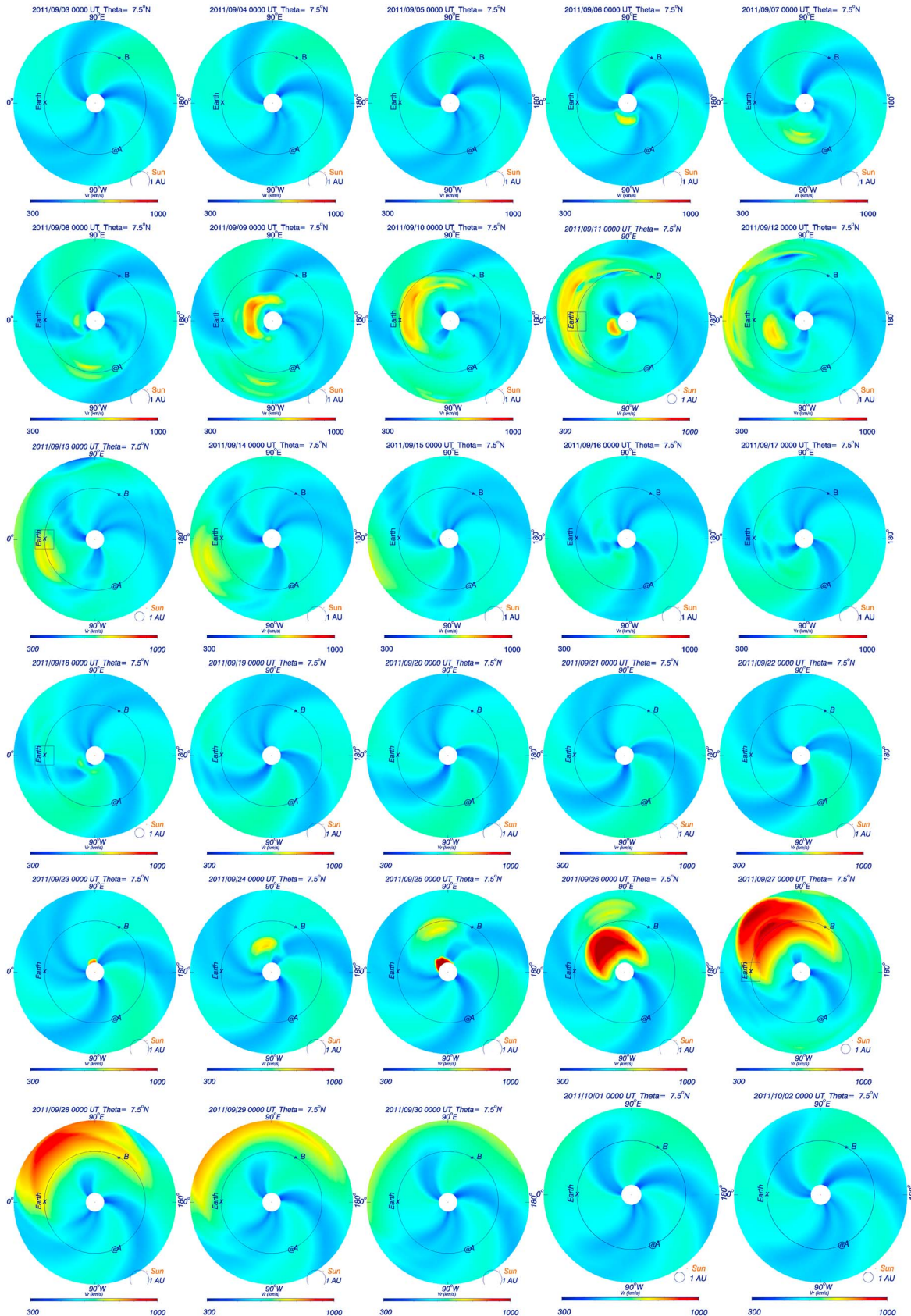
Figure 8. Simulated solar wind velocity near solar equator plane (latitude = 7.5° or 7.5°N) during 3 September to 2 October 2011. Note: Earth is at longitude = 0° in this figure.

Table 2. The Related Information for the Shock09's Candidate CMEs

Parameters	Shock09 at 1146 UT[a]			
	CME06a	CME06b	CME07a	CME07b
Driver of Shock09[b]	Yes-1	Yes-2	No	No
CME location (latitude and longitude)[c]	N14W07	N14W18	N23E54	N14W28
CME begin at (UT)[d]	0224	2239	1854	2254
V_{CME} at Cor2 (km/s)[e]	312	570	657	681
Estimated δt (h)[f]	131.80	72.23	62.59	60.38
Actual δt (h)[g]	81.37	62.62	40.87	36.87
V_{SW} at 1 AU (km/s)[h]	590	590	590	590
Estimated Δt (h)[i]	69.69	69.69	69.69	69.69
δt_{Error} (h)[j]	50.43	9.61	19.72	23.41
Δt_{Error} (h)[k]	−11.68	7.07	28.82	32.78

[a]Arrival time of Shock09 at 1 AU.
[b]Driver candidate for Shock09 in the first row.
[c]Driver's source location: latitude and longitude. For example, N14W07 means the source of the CME located at 14°N and 7°W.
[d]Time when CME was first seen by SECCHI/STEREO COR2A.
[e]CME propagation speed measured by COR2A.
[f]Estimated arrival time of CME's driven shock propagation time from $2\,R_S$ to Wind spacecraft using the CME speed measured by COR2A.
[g]Actual delay time for CME/shock propagation time from $2\,R_S$ to Wind.
[h]In situ solar wind speed (by Wind) at downstream of Shock09.
[i]Delay time for solar wind with speed listed in the eighth row to propagate from $\sim 2\,R_S$ to Wind.
[j]$\delta t_{Error} \equiv$ estimated δt − Actual δt (units in hours).
[k]$\Delta t_{Error} \equiv$ estimated Δt − actual δt (units in hours).

It is well known that the source location of solar disturbances is another factor that can affect the propagation of CMEs [e.g., *Wu et al.*, 2007a, 2007b, 2011]. Figure 8 shows clearly that the center of the CMEs did not pass the Earth on 11 or 27 September. But the center of the CME almost passed the Earth on 17 September. These simulation results verified the 1 AU in situ observations and explain (i) why there was no MC or MCL structure following IP Shock09 or Shock26 and (ii) IP Shock17 was followed by a MC.

5. Discussion

The solar source location is one of the major factors that affect the propagation of CMEs/ICMEs, which has been confirmed previously by using global 3-D MHD simulation [e.g., *Wu et al.*, 2007a, 2007b, 2011]. In September 2011, at least 12 CMEs were identified but only four clear IP shocks (Shock09, Shock17, Shock25, and Shock26) were identified from the Wind solar wind data set. Three (Shock09, Shock17, and Shock26) out of four IP shocks induced sizeable geomagnetic storms, which are all caused by the southward IMF in the sheath regions. We will discuss these three events in the following sections. We will now examine the associations of specific shocks with their possible solar sources and CMEs in the context of the global 3-D solar temporal variations.
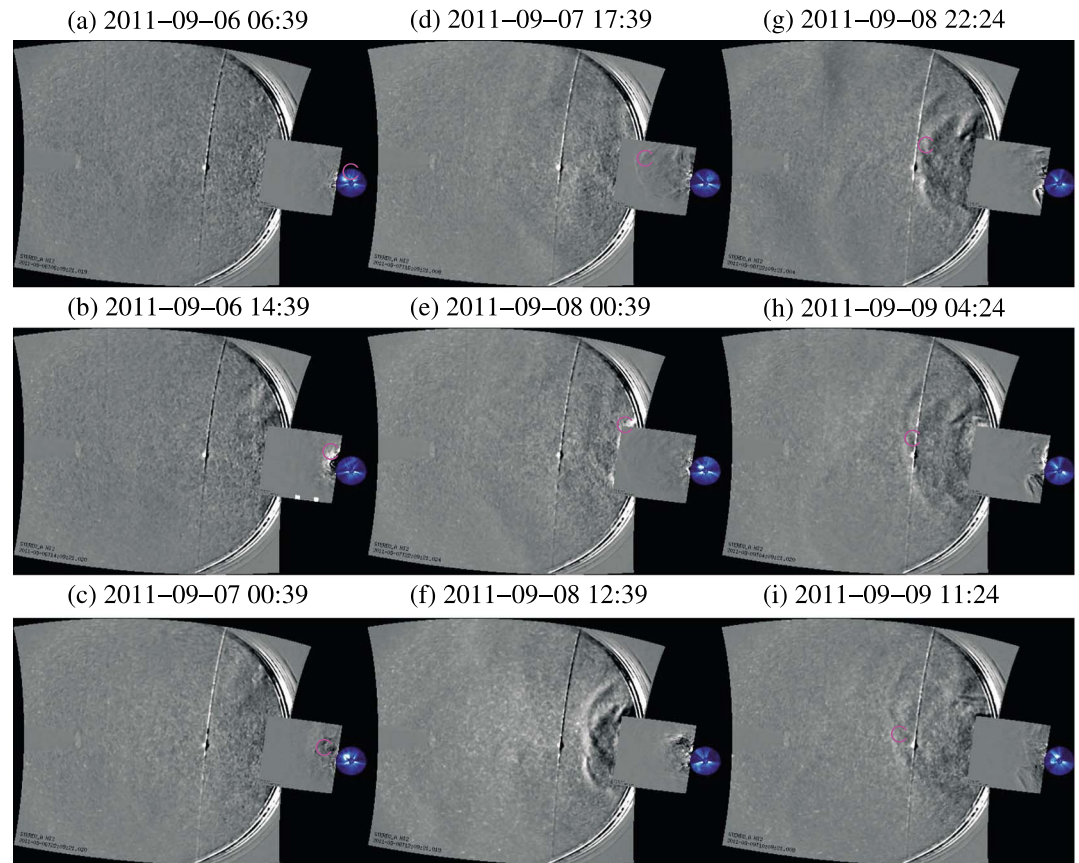
5.1. IP Shock on 9 September 2011: Shock09

Table 2 lists the possible four CME candidates that may drive the IP Shock09, information (source location, propagation speed) of the CMEs, estimated (and actual) arrival time at Wind for the CME-driven Shock09, and solar wind velocity (by Wind) at the downstream of Shock09.

As seen in Table 2, it would take 131.8, 72.23, 62.59, and 60.38 h (see estimated δt in Table 2) for CME6a, CME6b, CME7a, and CME7b to propagate from the Sun to the Wind (or Earth environment), respectively. The actual propagation time (actual δt in of Table 2) for CME6a, CME6b, CME7a, and CME7b to drive Shock09 to arrive at the Wind are 81.37, 62.62, 40.87, and 36.87 h. None of these four CMEs could drive an IP shock to arrive at 1 AU at 11:46 UT on 9 September because none of them are fast enough to arrive at Wind in time (see Table 2, δt_{Error} are 50.43, 9.61, 19.72, and 23.41 h for these four CME candidates). It is trivial to use solar wind speed to estimate the possible source region back to the Sun. For this case, using solar wind speed (at downstream of the Shock09 is 590 km s^{-1}), Δt_{Error} are −11.68, 7.07, 28.82, and 32.78 h (see in Table 2) for CME6a, CME6b, CME7a, and CME7b, respectively. Based on the measured near-Sun speeds, none of these CMEs were traveling fast enough to cause the observed Shock09. What is the source of IP Shock09? This question is examined in the following paragraphs.
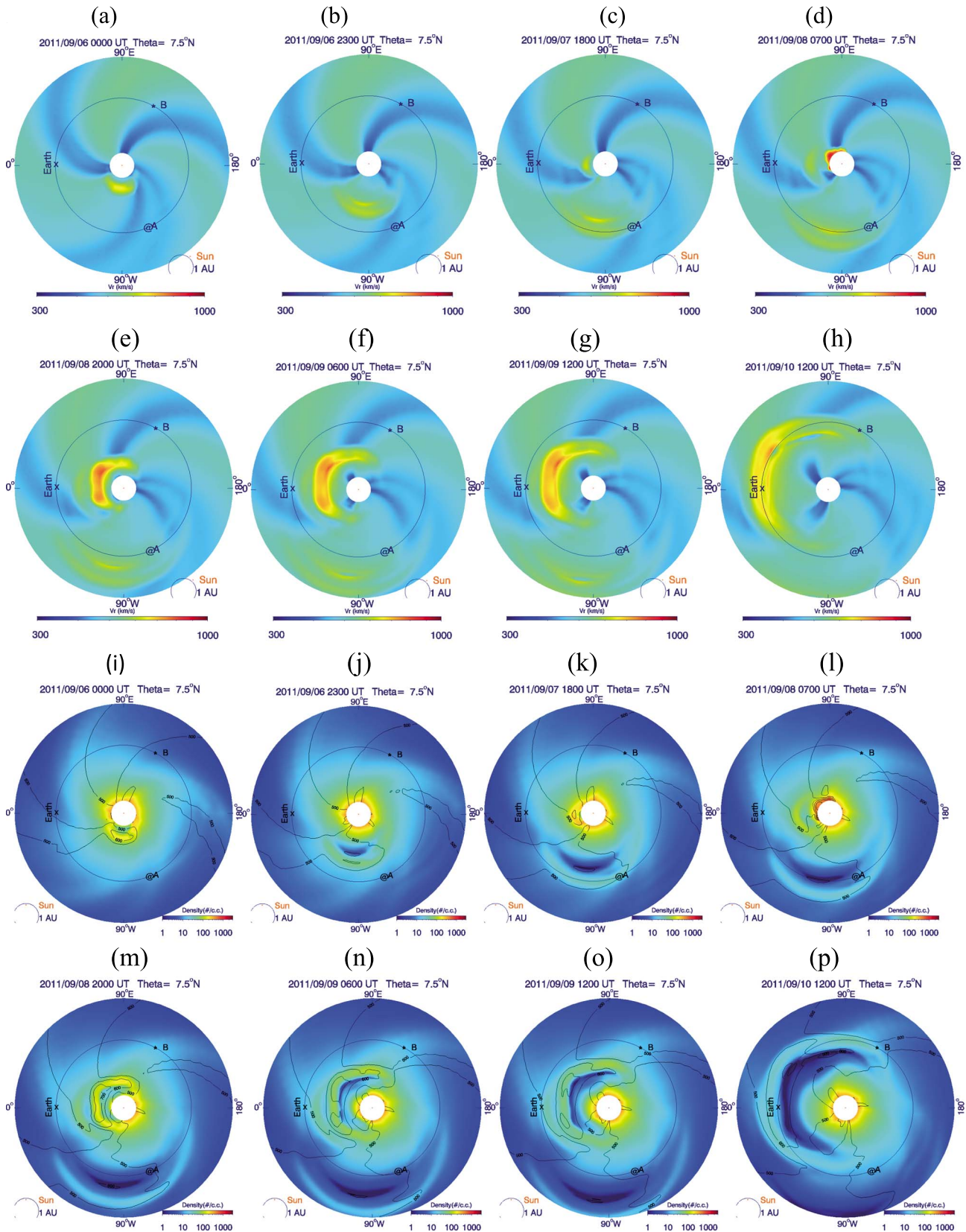
Figure 9. Time profile of (a–h) simulated solar wind velocity and (i–p) density in the plane of 7.5°N of solar equator. Black curves in Figures 9i–9p represent velocity contours. "x," "@," and "*," mean the location of the Earth, spacecraft of STEREO-A and STEREO-B, respectively.

(a) 2011−09−06 06:39   (d) 2011−09−07 17:39   (g) 2011−09−08 22:24

(b) 2011−09−06 14:39   (e) 2011−09−08 00:39   (h) 2011−09−09 04:24

(c) 2011−09−07 00:39   (f) 2011−09−08 12:39   (i) 2011−09−09 11:24

Figure 10. Combined COR2 (the circle shape in the middle at the right), HI1 (the smaller rectangular shape in the middle), and HI2 (the bigger rectangular shape at the left) coronagraphs during 6–9 September 2011. "C" marked the part of the CMEs/shocks. The Sun is at the center of the small blue circle and the Earth the dot at 1 AU on that vertical arc.

The source locations of these four CMEs are at N17W07, N14W18, N23E54, and N14W28, respectively. The source locations of CME06a and CME6b are close to the Sun-Earth line. CME06a was ejected into a region where the solar wind speed was higher than the surrounding area (see Figure 9c). According to in situ observation, the solar wind speed of the CME-driven shocks is normally higher than the speed of their drivers (MCs, MCLs, or ICMEs). An IP shock is normally driven by a driver of some sort (e.g., a MC, a MCL, or an ICME). The sheath is the area between the IP shock and its driver. The average duration of the sheath ahead of the MCs is about 12 h [*Wu and Lepping*, 2016]. For CME06b, both δt_{Error} (9.61 h) and Δt_{Error} (= 7.07 h) are shorter than 10 h: the estimated errors are ≈ 15% and 11%. Therefore, CME06b is the most likely driver for the IP Shock09. The observations from COR2A, HI-1, and HI-2 from STEREO-A also show similar results (see Figure 10.)

Figure 9 shows a time sequence of the solar wind profile at 7.5°N. It shows clearly that the front of the fast wind and the front of IP Shock09 arrived at the Earth at almost the same time (see Figures 9f and 9n). The IP Shock09 interacted with the front boundary of the fast wind, i.e., a CIR. The collision (or interaction) between the Shock09 and the CIR generated a special solar wind structure: jumps in solar wind velocity, IMF, and thermal speed are very small, but the jump in density is large (that is shown in Figures 1a and 2a). Figure 2a has a smaller time scale than Figure 1a. The red dashed line indicates the arrival time of the Shock09 at Wind. Therefore, we will conclude that CME06b is the most likely driver for Shock09 because δt_{Error} is 9.61 h and Δt_{Error} is 7.07 h. Either δt_{Error} or Δt_{Error} is shorter than the average duration of the sheath ahead of the MCs as described in the report by *Wu* and *Lepping* [2016]. Note that the CME-CME interaction can be classified into a complex ejecta [e.g., *Burlaga et al.*, 2002] and a multicloud structure [e.g., *Wang et al.*, 2003]. The CME-CME interaction is much more complex. There are various possibilities of interplanetary interaction among multiple CMEs. These kinds of interactions were discussed previously

Table 3. The Related Information for the Shock17's Candidate CMEs

Parameters	Shock17 at 0253 UT[a]	
	CME14a	CME14b
Driver of Shock17[b]	Yes	No
CME location (latitude, longitude)[c]	N22W03	S15W45
CME begin at (UT)[d]	0154	2154
V_{CME} at Cor2 (km/s)[e]	400	400
Estimated δt (h)[f]	102.8	102.8
Actual δt (h)[g]	72.98	52.98
V_{SW} at 1 AU (km/s)[h]	550	550
Estimated Δt (h)[i]	74.77	74.77
δt_{Error} (h)[j]	29.82	49.82
Δt_{Error} (h)[k]	1.79	21.78

[a]Arrival time of Shock17 at 1 AU.
[b]Driver candidate for Shock17 in the first row.
[c]Driver's source location: latitude and longitude. For example, N22W03 means the source of the CME located at 22°N and 03°W.
[d]Time when CME was first seen by SECCHI/STEREO COR2A.
[e]CME propagation speed measured by COR2A.
[f]Estimated arrival time of CME's driven shock propagation time from 2 R_S to Wind spacecraft using the CME speed measured by COR2A.
[g]Actual delay time for CME/shock propagation time from 2 R_S to Wind.
[h]In situ solar wind speed (by Wind) at downstream of Shock17.
[i]Delay time for solar wind with speed listed in eighth row to propagate from ~2 R_S to Wind.
[j]$\delta t_{Error} \equiv$ estimated $\delta t -$ actual δt (units in hours).
[k]$\Delta t_{Error} \equiv$ estimated $\Delta t -$ actual δt (units in hours).

by using the 2.5-D MHD simulation [e.g., *Xiong et al.*, 2006a, 2006b, 2007, 2009] and 3-D MHD simulation [e.g., *Wu et al.*, 2007b, 2012]. In Table 2, the CME06a and the CME06b erupted from two different locations of N14W07 and N14W18. Interaction of CME06a-CME06b is a kind of oblique collision [*Xiong et al.*, 2006b, 2009].

After the CMEs were injected into the inner heliosphere, the speed of the CMEs may increase or decrease. The deceleration/acceleration of CMEs depends on the relationship between the CMEs' propagation speed and the background solar wind speed. For example, previous studies show that most slow CMEs were accelerated, but most fast CMEs were decelerated en route to the Earth [e.g., *Shen et al.*, 2012; *Xie et al.*, 2013]. This kind of phenomena has been confirmed previously by using MHD simulation [e.g., *Wu et al.*, 2006a, 2007a, 2007b, 2011; *Liou et al.*, 2014]. If the background solar wind is faster than the propagation speed of the CME/ICME, the propagation speed of the CME/ICME will increase.

5.2. IP Shock on 17 September 2011: Shock17

On 17 September 2011, at ~02:53 UT and ~07:00 UT Wind recorded (Figure 1b) an IP shock (Shock17) and a density enhancement (or a magnetic hole, MH17). The density peak of the MH17 is $\approx 60\,\text{cm}^{-3}$ which is smaller than that for the MH09 ($Np_{peak} = 94\,\text{cm}^{-3}$). It is interesting to point out that the peak density of MH09 is ~40% higher than that for MH17. Table 3 lists the information for the Shock17 and its related drivers (i.e., candidate CMEs). There are two CME candidates that may have generated the Shock17. Table 3 shows, tentatively, that CME14a is the main driver for the IP Shock17: (i) The estimated Δt (= 74.77 h) is close to the actual δt (72.99 h) and (ii) the source location for CME14a is closer to the Sun-Earth line than that for CME14b. Figure 11 shows a time sequence of velocity profiles on a plane at 7.5 N° (Figures 11a–11h) and on the meridian plane along the Sun-Earth line (Figures 11i–11p). IP Shock17 arrived at the Earth (Figures 11g and 11o) several hours earlier than that for the front boundary of the CIR (Figures 11h and 11p). We examine the CME source in more detail in the next paragraph.

The source location of CME14a is at N22W03, which is close to the Sun-Earth line. Due to the effect of fast background solar wind, CME14a could have arrived at Wind earlier than the estimated arrival time (e.g., see the above section 5.1 for the Shock09). The observed solar wind speed downstream of Shock17 was ~550 km s^{-1} (see Table 3 or Figure 1b), which took about 74.765 h to arrive at 1 AU. Again, this event demonstrated another case in which a CME can be "accelerated" by the background solar wind whose speed is higher than the near-Sun speed of the CME, and the transporting duration of a slow CME can be shortened by its acceleration of the ambient solar wind [e.g., *Wang et al.*, 2004]. Since CME14a was ejected near the Sun-Earth line, the center of the ICME14a would cross the Wind spacecraft. This means that a MC should be observed at the Earth. This was confirmed by the observation: Wind recorded a MC [*Lepping et al.*, 2015b] following the Shock17. CME14a was riding in a region with fast solar wind (~500 km s^{-1}). Therefore, we conclude (Table 2) that CME14a is the source for Shock 17.

5.3. IP Shock on 26 September 2011: Shock26

Wind recorded an IP shock on 25 and 26 September 2011 (see Figure 4). Tables 4 and 5 list the related information for the Shock25 and Shock26, respectively. It is clear that CME22 is the driver for the Shock25
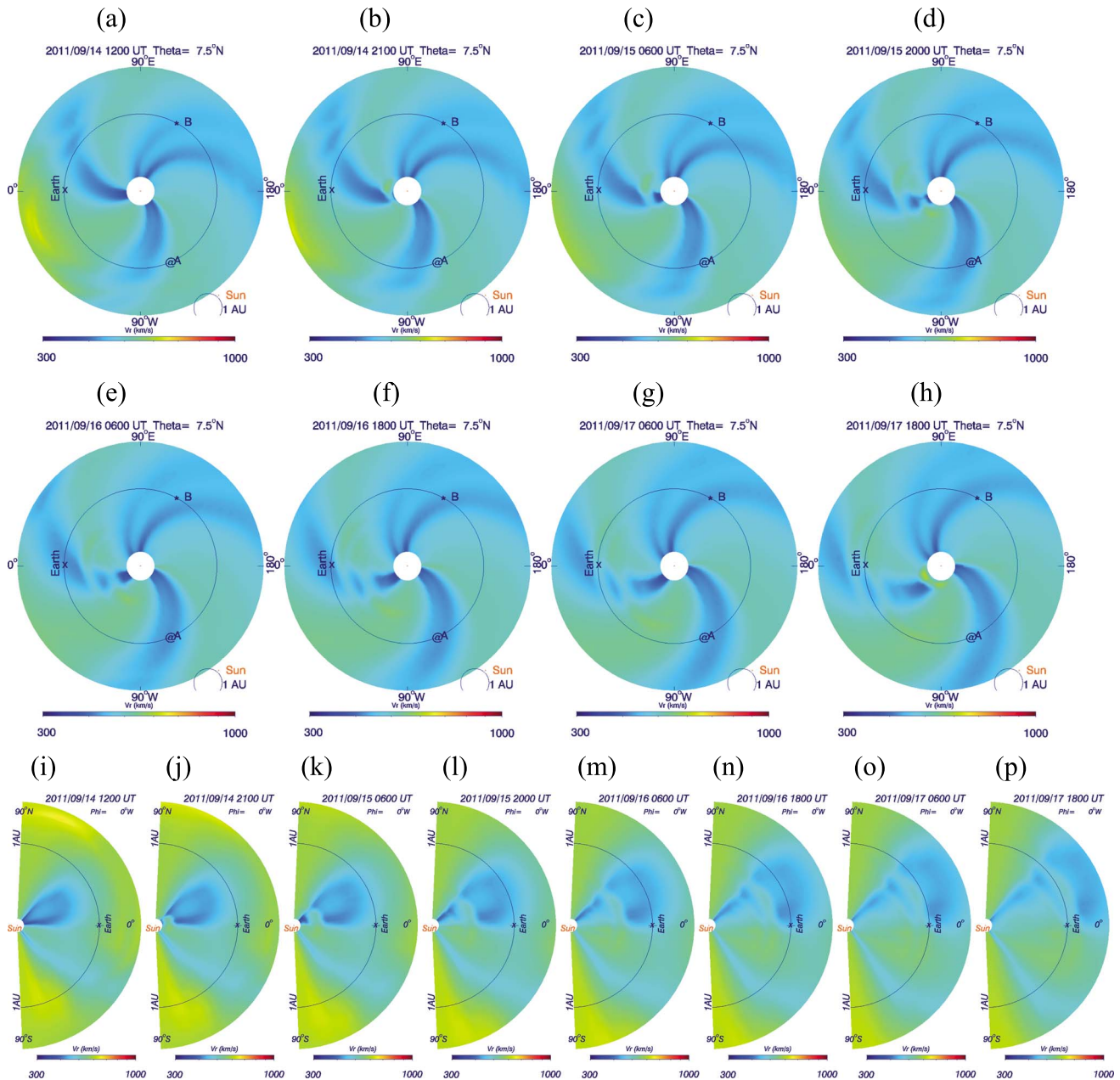
Figure 11. Time profile of simulated solar wind velocity in the plane of (a–h) 7.5°N of solar equator and (i–p) Sun-Earth meridian plane during 14–17 September 2011.

(see Figure 12). Table 4 shows a large δt_{Error} (−31.92 h) and Δt_{Error} (42 h) for CME22-driven shock to arrive at the Earth. The estimation of δt_{Error} is only good for a head-on event. Figure 9c shows the front boundary of the IP shock arrived at the 1 AU at 05 UT on 24 September 2011. It took about ~43.5 h for CME22 to arrive at 1 AU, which is close to estimated δt. (= 40.3 h), and the δt_{Error} is small (= 3.5 h). Source location of CME22 (N08E68) is far away from the Sun-Earth line. It took a longer time to arrive at the Earth (see Figure 8d).

Table 5 shows that both CME24a and CME24b are the two possible drivers for the Shock26. Figure 12 shows that the flank of the simulated IP shocks passed the Earth on 25 September (at 09 UT, see Figure 12d), and 26 September (at 12 UT, see Figure 12f), respectively. This matches the Wind in situ observation as shown in Figure 1c. The center of the simulated ICMEs/Shocks did not pass the Earth, which implies that no MC/MCL would be recorded at the Earth. This also matches the Wind observation: two IP shocks were recorded,

Table 4. The Related Information for the Shock25's Candidate CMEs

Parameters	Shock25 at 0936 UT		
	CME22	CME24a	CME24b
Driver of Shock25	Yes	No	No
CME location (longitude and latitude)	N08E68	N12E60	N12E60
CME begin at (UT)	0922	1254	1948
V_{CME} at Cor2 (km/s)	1020	1050	1065
Estimated δt (h)	40.3145	39.1627	38.6111
Actual δt (h)	72.23	20.07	13.80
V_{SW} at 1 AU (km/s)	360	360	360
Estimated Δt (h)	114.225	114.225	114.225
δt_{Error} (h)	−31.92	19.09	24.81
Δt_{Error} (h)	42.0	94.16	100.43

one on 25 September and the other on 26 September. Wind recorded Shock25 and Shock26 (Figure 1c) at 09:36 UT on 25 September and at 11:18 UT on 26 September, respectively.

No MC/MCL structure was identified following the IP Shock26 [*Lepping et al.*, 2012, 2015b; *Wu and Lepping*, 2015]. Shock26 induced an SSC and Dst_{min} dropped to −137 nT. The upstream and downstream speeds of Shock26 were ~350 km/s and ~450 km/s, respectively. The solar wind speed increased continuously to ~720 km/s ~8 h after Shock26 crossed the Wind spacecraft (see Figure 4b). After Shock26 crossed Wind, both θ_B and ϕ_B rotated a couple of times. Wind did not record a clear heliospheric plasma sheet (HPS) structure following the Shock26. The time sequence of *r*-phi plots near the solar equatorial plane (Figures 12e–12h) shows clearly that the CIR is far away from the Earth.

For the IP Shock26, the estimated arrival time of CME22 at 1 AU is ~03 UT on 25 September. The source location of CME22, N08E78, is far away from the Sun-Earth line; thus, the shock driven by CME22 could have arrived at Wind later than the estimation. The simulation results (Figure 12) confirm this assumption. CME24a and CME24b (source location at N12E60) are the two candidates that could drive the IP Shock26. The estimated delay time of CME24b (~39.50 h) matches the observation (~39.27 h). The shock driven by CME24a could have arrived at 1 AU a few (~6) hours later than that for the observation. In addition, simulation results also show that the two shocks driven by CME24a and CME24b were merged into one while they are en route to 1 AU. The merging of CME24a-CME24b is a kind of direct collision since both CME were ejected from the same source location [e.g., *Xiong et al.*, 2006a, 2007].

The resolution of the computational grid is $103 \times 36 \times 72$ which is rather low, especially in the radial direction with only 103 grid points to cover the range from 40 to 346 solar radii. The grid resolution in the radial direction is capable of constructing a fast shock wave. Recently, using simulation results made by the H3DMHD model, we are able to trace interplanetary fast shocks while the shock waves were propagating away from the Sun to 1 AU and found the following: (i) the strength (Mach number) of IP fast shocks (M_{fast}) is affected by the background solar wind for the shock driven by an extremely fast CME ($V_{CME} > 3000$ km/s) which occurred on 23 July 2012 [*Liou et al.*, 2014] and (ii) time-profile intensity of solar

Table 5. The Related Information for the Shock26's Candidate CMEs

Parameters	Shock26 at 1118 UT		
	CME22	CME24a	CME24b
Driver of Shock26	No	Yes	Yes
CME location (latitude and longitude)	N08E68	N12E60	N12E60
CME begin at (UT)	0922	1254	1948
V_{CME} at Cor2 (km/s)	1020	1050	1065
Estimated δt (h)	40.31	39.16	38.61
Actual δt (h)	99.07	46.40	39.50
V_{SW} at 1 AU (km/s)	730	730	730
Estimated Δt (h)	56.33	56.33	56.33
δt_{Error} (h)	−58.76	−7.24	−0.89
Δt_{Error} (h)	−42.74	9.93	16.82
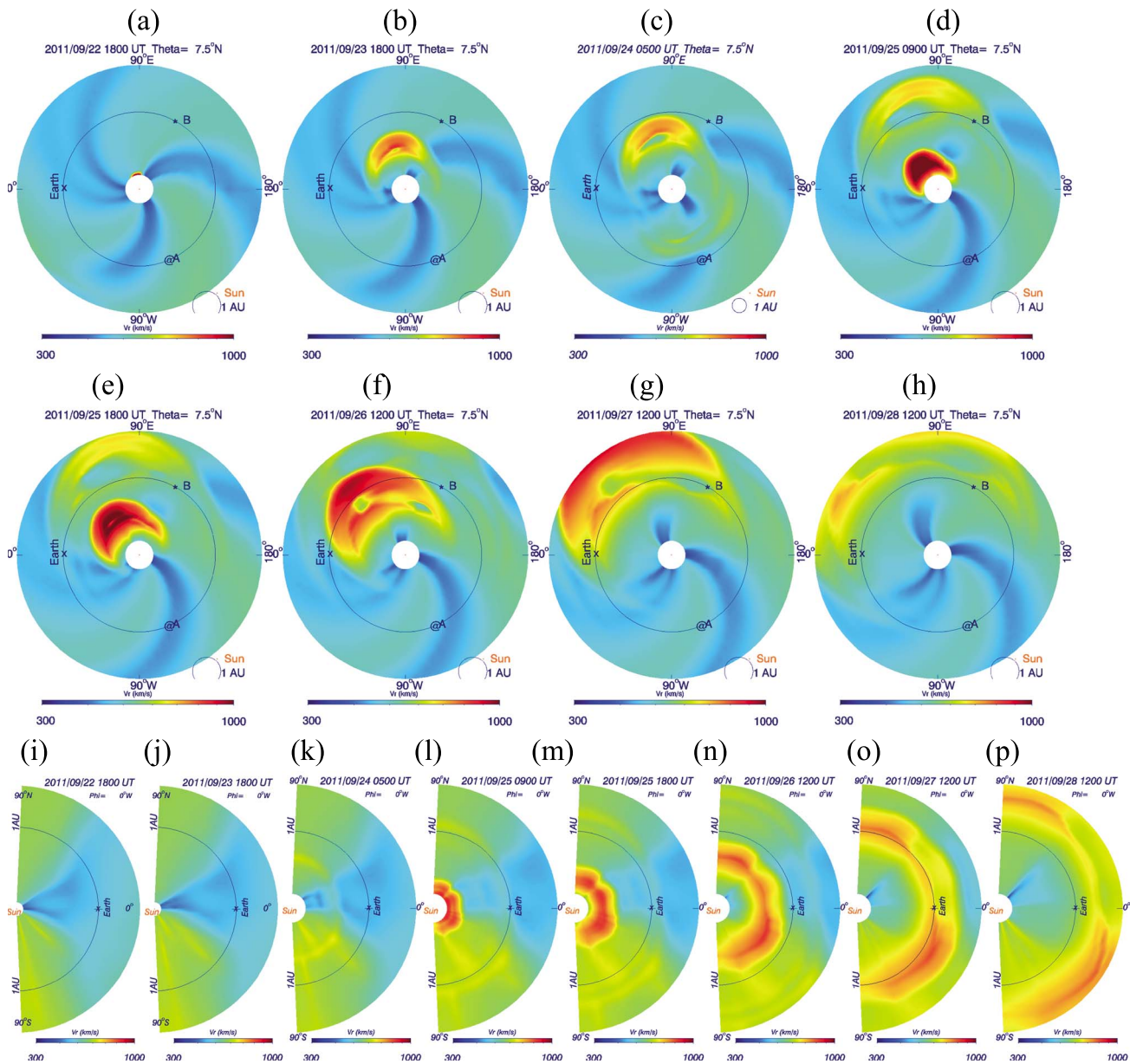
Figure 12. Time profile of simulated solar wind velocity in the plane of (a–h) 7.5°N of solar equator and (i–p) Sun-Earth meridian plane during 22–28 September 2011.

energetic particles and M_{fast} is correlated for IP shocks driven by a moderate CME (V_{CME} ~1000 km/s) that occurred on 15 March 2013 [*Wu et al.*, 2016].

6. Conclusion and Remarks

This study performs a simulation example of multiple coronal mass ejections (12 CMEs) and CME-driven shocks propagating as realistic 3-D solar wind structures from the Sun to the Earth in September 2011. In this study, we use the observed CMEs' speeds and source locations as constraints for the simulation inputs and compare with in situ solar wind data at 1 AU for tuning the simulation results. This procedure made the simulation results more realistic.

In this study, we demonstrated that the global 3-D simulation (H3DMHD) model is a useful tool for performing (1) the prediction of CME/Shocks' arrival time at the Earth; (2) whether the drivers of the IP shocks will be observed behind the shocks; and (3) the interaction between different solar wind structures

(e.g., CMEs, shocks, and sector boundaries). Item (2) is, of course, important for space weather forecasting prediction accuracy.

We believe that this hybrid simulation procedure can provide a tool to link the general cases of ICME at 1 AU to their solar sources, as well as to identify the possible origins of shock formation due to CME and CME/CIR interaction, and to timing the crossing of sector boundary information. As noted above, the interplanetary medium can contain a plethora of structures such as CMEs, shocks, sector boundaries, magnetic holes, MCs, and MCLs. Thus, we must finally note that in some cases such as the present study, it may be necessary to simulate a long period of time (here September 2011) in order to make more realistic solar event geomagnetic storm commencement associations with the use of 3-D MHD methodology.

A global H3DMHD simulation model can be used as a tool for space weather. For example, it is capable of predicting the arrival of CME-driven shocks at the Earth [*Zhao and Dryer*, 2014], variations of solar wind speed, density, temperature, and total magnetic field (see Figure 4). It is well established that the southward component of IMF plays a major role in geomagnetic activity. This is one of the elements that our H3DMHD cannot provide, as a realistic 3-D magnetic flux rope model is still not available. We intend to address this defect in our future work.

References

Arge, C. N., and V. J. Pizzo (2000), Improvement in the prediction of solar wind conditions using near-real time solar magnetic field updates, *J. Geophys. Res.*, *105*, 10,465–10,479, doi:10.1029/1999JA000262.

Akasofu, S.-I. (1981), Energy coupling between the solar wind and the magnetosphere, *Space Sci. Rev.*, *28*, 121–190.

Burlaga, L. F., E. Sittler, F. Mariani, and R. Schwenn (1981), Magnetic loop behind an interplanetary shock: Voyager, Helios, and IMP 8 observations, *J. Geophys. Res.*, *86*, 6673–6684, doi:10.1029/JA086iA08p06673.

Burlaga, L. F., S. P. Plunkett, and O. C. S. Cyr (2002), Successive CMEs and complex ejecta, *J. Geophys. Res.*, *107*(A10), 1266, doi:10.1029/2001JA000255.

Detman, T. R., M. Dryer, T. Yeh, S. M. Han, and S. T. Wu (1991), A time-dependent, three-dimensional MHD numerical study of interplanetary magnetic draping around plasmoids in the solar wind, *J. Geophys. Res.*, *96*, 9531–9540, doi:10.1029/91JA00443.

Fry, C. D., W. Sun, C. S. Deehr, M. Dryer, Z. Smith, S.-I. Akasofu, M. Tokumaru, and M. Kojima (2001), Improvements to the HAF solar wind model for space weather predictions, *J. Geophys. Res.*, *106*(A10), 20,985–21,002, doi:10.1029/2000JA000220.

Gopalswamy, N., P. Makela, H. Xie, S. Akiyama, and S. Yashiro (2009), CME interactions with coronal holes and their interplanetary consequences, *J. Geophys. Res.*, *114*, A00A22, doi:10.1029/2008JA013686.

Han, S. M. (1977), A numerical study of two dimensional time-dependent magnetohydrodynamic flows In: PhD Thesis, Univ. of Alabama in Huntsville.

Han, S. M., S. T. Wu, and M. Dryer (1988), A three-dimensional, time-dependent numerical modeling of super-sonic, super-Alfvénic MHD flow, *Comput. Fluids*, *16*, 81–103.

Hayashi, K., M. Tokumaru, K. Fujiki, and M. Kojima (2011), Three-dimensional solar wind structures obtained with MHD simulation model using observation-based time-varying inner boundary map paper presented at 10th ASP Conference, Astron. Soc. of the Pac., Kaanapali, Hawaii, 13–18 March.

Lax, P. D., and B. Wendroff (1960), Systems of conservation laws, *Comm. Pure. Appl. Math.*, *13*, 217–237.

Lepping, R. P., C. C. Wu, D. B. Berdichevsky, and A. Szabo (2011), Magnetic clouds at/near the 2007–2009 solar minimum: Frequency of occurrence and some unusual properties, *Sol. Phys.*, *274*(1–2), 345–360.

Lepping, R. P., C. C. Wu, and D. B. Berdichevsky (2012), Model parameter fittings and characterizations of *Wind* magnetic clouds for the period from early 2007 to Fall 2012 American Geophysical Union, Fall Meeting 2012, Abstract SH41B-2109.

Lepping, R. P., C. C. Wu, and D. B. Berdichevsky (2015a), Yearly comparison of magnetic cloud parameters, sunspot number, and interplanetary quantities for the first 18 years of the *Wind* mission, *Sol. Phys.*, *290*, 553–578, doi:10.1007/s11207-014-0622-7.

Lepping, R. P., C. C. Wu, D. B. Berdichevsky, and A. Szabo (2015b), *Wind* magnetic clouds for years 2010–2012: Model parameter fittings, associated shock waves and comparisons to earlier periods, *Sol. Phys.*, *290*, 2265–2290.

Liou, K., C.-C. Wu, M. Dryer, S.-T. Wu, N. Rich, S. Plunkett, L. Simpson, C. D. Fry, and K. Schenk (2014), Global simulation of extremely fast coronal mass ejection on 23 July 2012, *J. Atmos. Sol. Terr. Phys.*, *121*, 32–41.

Lugaz, N., and II. Roussev (2011), Numerical modeling of interplanetary coronal mass ejections and comparison with heliospheric images, *J. Atmos. Sol. Terr. Phys.*, *73*(10), 1187–1200, doi:10.1016/j.jastp.2010.09.016.

Manchester, W. B., T. I. Gombosi, I. Roussev, A. Ridley, D. D. Zeeuw, I. V. Sokolov, K. G. Powell, and G. Toth (2004), Modeling a space weather event from the Sun to the Earth: CME generation and interplanetary propagation, *J. Geophys. Res.*, *109*, A02107, doi:10.1029/2003JA010150.

Möstl, C., et al. (2012), Multi-point shock and flux rope analysis of multiple interplanetary coronal mass ejections around 2010 August 1 in the inner heliosphere, *Astrophys. J.*, *758*(10), 18.

Odstrcil, D., V. J. Pizzo, and C. N. Arge (2005), Propagation of the 12 May 1997 interplanetary coronal mass ejection in evolving solar wind structures, *J. Geophys. Res.*, *110*, A02106, doi:10.1029/2004JA010745.

Shen, F., X. S. Feng, S. T. Wu, C. Q. Xiang, and W. B. Song (2011a), Three-dimensional MHD simulation of the evolution of the April 2000 CME event and its induced shocks using a magnetized plasma blob model, *J. Geophys. Res.*, *116*, A04102, doi:10.1029/2010JA015809.

Shen, C., Y. Wang, B. Gui, P. Ye, and S. Wang (2011b), Kinematic Evolution of a slow CME in coronal viewed by STEREO-B on 8 October 2007, *Sol. Phys.*, *269*, 389–400.

Shen, F., S. T. Wu, X. S. Feng, and C. C. Wu (2012), Acceleration and deceleration of coronal mass ejections during propagation and interaction, *J. Geophys. Res.*, *117*, A11101, doi:10.1029/2012JA017776.

Shen, F., C. Shen, J. Zhang, P. Hess, Y. Wang, X. Feng, H. Cheng, and Y. Yang (2014a), Evolution of the 12 July 2012 CME from the Sun to the Earth: Data-constrained three-dimensional MHD simulations, *J. Geophys. Res. Space Physics*, *119*, 7128–7141, doi:10.1002/2014JA020365.

Shen, C., Y. Wang, Z. Pan, B. Miao, P. Ye, and S. Wang (2014b), Full-halo coronal mass ejections: Arrival at the Earth, *J. Geophys. Res. Space. Physics*, *119*, 5107–5116, doi:10.1002/2014JA020001.

Tsurutani, B. T., E. J. Smith, W. D. Gonzalez, F. Tang, and S. I. Akasofu (1988), Origin of interplanetary southward magnetic fields responsible for major magnetic storms near solar maximum (1978–1979), *J. Geophys. Res.*, *93*, 8517.

Tsurutani, B. T., and W. D. Gonzalez (1997), in *The Interplanetary Causes of Magnetic Storms: A Review, Geophys. Monogr. Ser.*, vol. 98, edited by B. T. Tsurutani, W. D. Gonzalez, and Y. Kamide, pp. 77–89, AGU, Washington, D. C.

Wang, Y.-M., and N. R. Sheeley Jr. (1990a), Magnetic flux transport and the sunspot-cycle evolution of coronal holes and their wind streams, *Astrophys. J. Part 1*, *365*, 372–386.

Wang, Y.-M., and N. R. Sheeley Jr. (1990b), Solar wind speed and coronal flux-tube expansion, *Astrophys. J. Part 1*, *355*, 726–732.

Wang, Y.-M., and N. R. Sheeley Jr. (1992), On potential field models of the solar corona, *Astrophys. J.*, *392*, 310.

Wang, Y. M., P. Z. Ye, and S. Wang (2003), Multiple magnetic clouds: Several examples during March–April 2001, *J. Geophys. Res.*, *108*(A10), 1370, doi:10.1029/2003JA009850.

Wang, Y. M., C. Shen, S. Wang, and P. Z. Ye (2004), Deflection of coronal mass ejection in the interplanetary medium, *Sol. Phys.*, *222*, 329–343.

Wang, Y., B. Wang, C. Shen, F. Shen, and N. Lugaz (2014), Deflected propagation of a coronal mass ejection from the corona to interplanetary space, *J. Geophys. Res. Space Physics*, *119*, 5117–5132, doi:10.1002/2013JA019537.

Wood, B. E., C.-C. Wu, R. A. Howard, D. G. Socker, and A. P. Rouillard (2011), Empirical reconstruction and numerical modeling of the first geoeffective coronal mass ejection of solar cycle 24, *Astrophys. J.*, *729*, 70, doi:10.1088/0004-637X/729/1/70.

Wood, B. E., C.-C. Wu, A. P. Rouillard, R. A. Howard, and D. G. Socker (2012), A coronal Holes's effects on CME shock morphology in the inner heliosphere, *Astrophys. J.*, *755*, doi:10.1088/0004-637X/755/1/43.

Wu, C.-C., and R. P. Lepping (2016), Relationships Among Geomagnetic Storms, Interplanetary Shocks, Magnetic Clouds, and Sunspot Number during 1995–2012, *Sol. Phys.*, *291*, 265–284, doi:10.1007/s11207-015-0806-9.

Wu, C.-C., J. K. Chao, S. T. Wu, and M. Dryer (1996), Numerical simulation of interplanetary slow shocks in the solar wind, *Sol. Phys.*, *165*, 377–393.

Wu, C.-C., S. T. Wu, and M. Dryer (2004), Evolution of fast and slow shock interactions in the inner heliosphere, *Sol. Phys.*, *223*, 259–282.

Wu, C.-C., X. S. Feng, S. T. Wu, M. Dryer, and C. D. Fry (2006a), Effects of the interaction and evolution of interplanetary shocks on "background" solar wind speeds, *J. Geophys. Res.*, *111*, A12104, doi:10.1029/2006JA011615.

Wu, C.-C., C. D. Fry, S. T. Wu, M. Dryer, and K. Liou (2007a), Three-dimensional global simulation of ICME propagation from Sun to the heliosphere, *J. Geophys. Res.*, *112*, A09104, doi:10.1029/2006JA012211.

Wu, C.-C., C. D. Fry, S. T. Wu, M. Dryer, B. Thompson, K. Liou, and X. S. Feng (2007b), Three-dimensional global simulation of multiple ICMEs' interaction and propagation from the Sun to the heliosphere following the 25–29 October solar events, *Adv. Space Sci. Rev.*, *40*, 1827–1834, doi:10.1016/j.asr.2007.06.025.

Wu, C.-C., M. Dryer, S. T. Wu, B. E. Wood, C. D. Fry, K. Liou, and S. Plunkett (2011), Global three-dimensional simulation of the interplanetary evolution of the observed geoeffective coronal mass ejection during the epoch 1–4 August 2010, *J. Geophys. Res.*, *116*, A12103, doi:10.1029/2011JA016947.

Wu, C.-C., K. Liou, S. T. Wu, M. Dryer, C. D. Fry, and S. Plunkett (2012), Heliospheric three-dimensional global simulation of multiple interacting coronal mass ejections during the Halloween 2003 epoch, *AIP Conf. Proc.*, *1436*, 285.

Wu, C.-C., K. Liou, A. Vourlidas, S. Plunkett, M. Dryer, S. T. Wu, and R. A. Mewaldt (2016), Global magnetohydrodynamic simulation of the March 15, 2013 coronal mass ejection event—Interplanetary of the 30–80 MeV proton flux, *J. Geophys. Res. Space Physics*, *121*, doi:10.1002/2015JA021051.

Wu, C.-C., and, R. P. Lepping (2002a), Effects of magnetic clouds on the occurrence of geomagnetic storms: The first 4 years of *Wind*, *J. Geophys. Res.*, *107*(A10), 1314, doi: 10.1029/2001JA000161.

Wu, C.-C., R. P. Lepping (2002b), Effect of solar wind velocity on magnetic cloud-associated magnetic storm intensity, *J. Geophys. Res.*, *107*(A11), 1346, doi: 10.1029/2002JA009396.

Wu, C. C., R. P. Lepping, and N. Gopalswamy (2006b), Relationship among magnetic clouds, CMEs, and Geomagnetic Storms, *Sol. Phys.*, *239*, 449–460.

Wu, C. C., and R. P. Lepping (2011), Statistical comparison of magnetic clouds with interplanetary coronal mass ejections for solar cycle 23, *Sol. Phys.*, *269*, 141–153.

Wu, C. C., and R. P. Lepping (2015), Statistical comparison of magnetic clouds and cloud-like structures during 1995–2012, *Sol. Phys.*, doi:10.1007/s11207-015-0656-5.

Xie, H., O. C. St. Cyr, N. Gopalswamy, D. Odstrcil, and H. Cremades (2013), Understanding shock dynamics in the inner heliosphere with modeling and type II radio data: A statistical study, *J. Geophys. Res. Space Physics*, *118*, 4711–4723, doi:10.1002/jgra.50444.

Xiong, M., H. Zheng, Y. Wang, and S. Wang (2006a), Magnetohydrodynamic simulation of the interaction between interplanetary strong shock and magnetic cloud and its consequent geoeffectiveness, *J. Geophys. Res.*, *111*, A08105, doi:10.1029/2005JA011593.

Xiong, M., H. Zheng, Y. Wang, and S. Wang (2006b), Magnetohydrodynamic simulation of the interaction between interplanetary strong shock and magnetic cloud and its consequent geoeffectiveness: 2. Oblique collision, *J. Geophys. Res.*, *111*, A11102, doi:10.1029/2006JA011901.

Xiong, M., H. Zheng, S. T. Wu, Y. Wang, and S. Wang (2007), Magnetohydrodynamic simulation of the interaction between two interplanetary magnetic clouds and its consequent geoeffectiveness, *J. Geophys. Res.*, *112*, A11103, doi:10.1029/2007JA012320.

Xiong, M., H. Zheng, and S. Wang (2009), Magnetohydrodynamic simulation of the interaction between two interplanetary magnetic clouds and its consequent geoeffectiveness: 2. Oblique collision, *J. Geophys. Res.*, *114*, A11101, doi:10.1029/2009JA014079.

Zhao, X., and M. Dryer (2014), Current status of CME/shock arrival time prediction, *Space Weather*, *12*, 14–35, doi:10.1002/2014SW001060.

Zhou, Y. F., and X. S. Feng (2013), MHD numerical study of the latitudinal deflection of coronal mass ejection, *J. Geophys. Res. Space Physics*, *118*, 6007–6018, doi:10.1002/2013JA018976.